Energy & Environmental Science

Accepted Manuscript

ROYAL SOCIETY OF CHEMISTRY

www.rsc.org/ees

Energy & Environmental Science

COMMUNICATION

Amorphous S-rich $S_{1-x}Se_x$/C (x≤0.1) Composites Promise Better Lithium Sulfur Batteries in Carbonate-based Electrolyte

Received 00th January 20xx,
Accepted 00th January 20xx

DOI: 10.1039/x0xx00000x

www.rsc.org/

Xiaona Li, Jianwen Liang, Kailong Zhang, Zhiguo Hou, Wanqun Zhang, Yongchun Zhu,* and Yitai Qian*

Polysulfide dissolution and insulating nature of sulfur cause significant capacity fading and low efficiency in rechargeable lithium-sulfur batteries. Here, we show that these defects can be effectively diminished by immobilize sulfur in porous carbon via the interaction of small amount of selenium. Amorphous S-rich $S_{1-x}Se_x$/C (x≤0.1) composites has been prepared starting from Se and S powders at 260 °C. Raman spectra reveal the existence of S-Se bonds in $S_{1-x}Se_x$/C composites. As cathodes for lithium-sulfur batteries, $S_{1-x}Se_x$/C (x≤0.1) composites exhibit high electrochemical performance in carbonate-based electrolyte. $S_{0.94}Se_{0.06}$/C deliver the best performance with a capacity of 910 mAh g^{-1} at 1 A g^{-1} over 500 cycles, 1105 mAh g^{-1} at 0.2 A g^{-1} after 100 cycles and good rate capability of 617 mAh g^{-1} at 20 A g^{-1}.

Lithium–sulfur (Li-S) batteries are regaining increasing interest since the concept emerged in 1960s[1], due to their high specific capacity (1675 mAh g^{-1}) and natural abundance of sulfur.[2-4] However, sulfur-based cathodes face the problems of the insulting property and the dissolution of polysulfide intermediate, which leads to the low electrochemical utilization of sulfur and fast capacity fading.[5-7]

Many efforts and significant achievements have been made over the last few years to solve these problems. The approach commonly adopted is immobilize sulfur in various materials (inorganic materials,[8, 9] polymers,[10] porous carbon[11]), to provide conductivity and alleviate the dissolution phenomenon. Nazar et al. firstly prepared sulphur/mesoporous-carbon composites, which exhibited reversible capacity about 1100 mAh g^{-1} at 168 mA g^{-1} after 20 cycles in ethyl methyl sulphone.[12] Recently, a conductive MXene phase Ti_2C was introduced as new host for Li-S batteries, the 70 wt% S/Ti_2C composites delivered a capacity of 723 mAh g^{-1} after 650 cycles at 837 mA g^{-1}.[13] Using small sulfur allotropes (S_{2-4})[14] and monoclinic sulfur[7] also have been proved as an effective way to avoid the formation of soluble polysulfides. For example, small S_{2-4} (~40 wt%) confined in microporous carbon exhibited 1142 mAh g^{-1} after 200 cycles at 167 mA g^{-1} in carbonate-based electrolyte.[14]

In 2012, Amine obtained SeS_2/carbon nanotubes composites starting from commercial SeS_2 at 160 °C,[15] delivering 512 mAh g^{-1} at 50 mA g^{-1} after 30 cycles. Subsequently, SeS_2 and SeS_7/carbon nanotubes composites have been prepared by heating the compounds of SeS_2 and SeS_7 at 160°C,[16] exhibiting a discharge capacity of 571 and 833 mAh g^{-1} at 50 mA g^{-1} after 50 cycles, respectively. $SeS_{0.7}$/C composites with rich Se were prepared from SeS_2 annealed with polyacrylonitrile at 600 °C, which exhibited a capacity of 780 mAh g^{-1} at 0.6 A g^{-1} for 1200 cycles in carbonate-based electrolyte.[17]

Herein, we prepared several S-rich $S_{1-x}Se_x$/C (x ≈ 0.1, 0.08, 0.06, 0.05) composites starting from elemental S and Se powder at 260 °C. Raman spectra and X-ray photoelectron spectroscopy analysis reveal the existence of strong interaction between Se and S in the composites. On account of the stabilization effect, better conductivity of Se and the high capacity of S, the as-prepared S-rise $S_{1-x}Se_x$/C composites exhibit high electrochemical performance of Li-S batteries in carbonate-based electrolyte. Among them, $S_{0.94}Se_{0.06}$/C composites deliver a capacity of 910 mAh g^{-1} at 1 A g^{-1} over 500 cycles, 1090 mAh g^{-1} at 0.2 A g^{-1} after 200 cycles, and good rate capability of 617 mAh g^{-1} at 20 A g^{-1}. Moreover, compared with the S/C composite cathodes in the same approach, the as-prepared S-rich $S_{1-x}Se_x$/C (x≤0.1) composites exhibit an extremely small plateau at 2.5 V in the first cycle and single stable platea at ~2.0 V from the 2nd cycle, which demonstrate the effective reduction of the large polysulfides formation during the cycling.

In a typical synthesis of S-rich $S_{1-x}Se_x$/C (x ≈ 0.1, 0.08, 0.06, 0.05) composites, the mixture of elemental sulfur and selenium powders with related molar ratio were firstly ball-milled with porous carbon (carbon content 50 wt%) we prepared (the morphology and pore-size distribution shown in Fig. S1a-c, see the Supporting Information). Subsequently, the ball-milled

Hefei National Laboratory for Physical Science at Micro-scale, Department of Chemistry,
University of Science and Technology of China
Hefei, Anhui 230026, (P. R. China)
E-mail: ytqian@ustc.edu.cn, ychzhu@ustc.edu.cn.
Electronic Supplementary Information (ESI) available. See DOI: 10.1039/x0xx00000x

precursor was fully filled in a 5 ml autoclave and heated for 24 h. Considering the high melting point of Se (221 °C), to make Se, S be fully miscible with each other, we chose 260 °C as the reaction temperature. Then the products labeled as $S_{1-x}Se_x$/C (x = 0.05, 0.06, 0.08, 0.1) are obtained, and here we take $S_{0.94}Se_{0.06}$/C as an example (the molar ratio of raw material S and Se is 15:1).

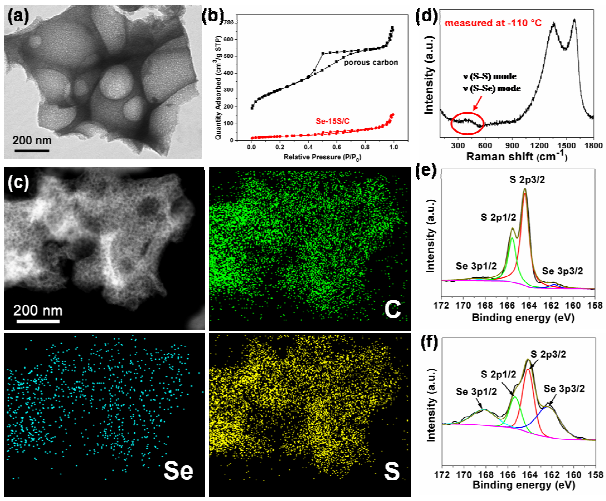

Fig. 1 (a) TEM image of $S_{0.94}Se_{0.06}$/C sample. (b) Adsorption–desorption isotherms of porous carbon and $S_{0.94}Se_{0.06}$/C sample. (c) STEM image, C, Se and S elemental mapping of $S_{0.94}Se_{0.06}$/C sample. (d) Raman spectrum of $S_{0.94}Se_{0.06}$/C recorded at about -110 °C. (e,f) XPS spectra of S 2p and Se 3p in the $S_{0.94}Se_{0.06}$/C sample before and after heat treatment.

The transmission electron microscopy (TEM) images of the $S_{0.94}Se_{0.06}$/C sample before and after the reaction are shown in Fig. S2 and Fig. 1a, respectively. It can be seen that the disappeared of bulk Se or S powder after reaction. The Brunaure-Emmett-Teller (BET) measurement (Fig. 1b) exhibits that the surface area and pore volume of $S_{0.94}Se_{0.06}$/C sample decrease sharply compared to the of carbon host (from 1069 $m^2\ g^{-1}$ and 1.13 $cm^3\ g^{-1}$ to 89 $m^2\ g^{-1}$ and 0.17 $cm^3\ g^{-1}$), indicating the impregnation of large portion of Se and S into the carbon host.[18, 19] Thermogravimetric analysis suggests that the carbon contents in the final composites are all about 50 wt%, indicating no noticeable evaporation of S and Se during the heat process. The elemental analysis indicates the molar proportion of S to Se loading is about 94 % and 6%, respectively, which is close to that of the raw material (Fig. S3 and Table S1).

The uniform distribution of Se and S is evidenced by elemental mapping (Fig. 1c, EDS spectra shown in Fig. S4). In the Raman spectra recorded at room temperature (Fig. S5a), apart from the two bands ascribed to carbon host, no obvious peaks are observed. That is due to the confined effect of porous carbon,[11, 20] thus also confirm the well done infiltration process. While for the spectra recorded at -110 °C (Fig. 1d and Fig. S5b for other $S_{1-x}Se_x$/C samples), there're some small peaks around 400 cm^{-1}, which are induced from the stretching vibrations of S-Se (~360 cm^{-1}), S-S (~470 cm^{-1}) bonds.[21, 22] In order to excluding interferences of the carbon host, the Raman spectra recorded at liquid state (using CS_2 as solvent) of those samples are also obtained (Fig. S5c, the Raman spectrum of CS_2 is shown in Fig. S5d), giving the direct evidence of those bonds in the composites. Moreover, the X-ray photoelectron spectroscopy (XPS) spectra of high-resolution S2p and Se3p before and after the reaction are shown in Fig. 1e,f. The enhanced peaks of Se 3p and the larger overlapped regions of the latter one also validate the interreaction between Se and S in the $S_{0.94}Se_{0.06}$/C sample[17].

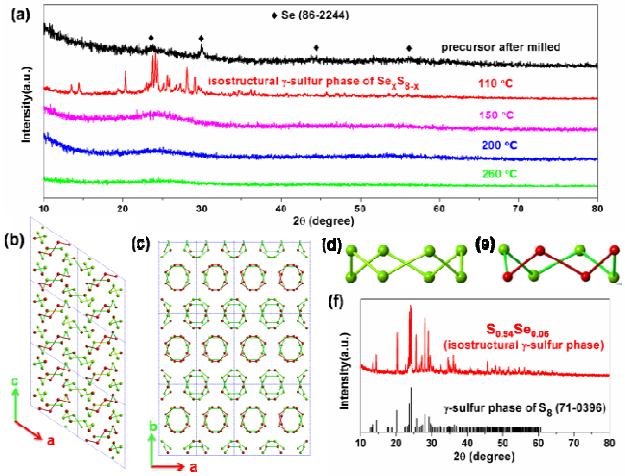

Fig. 2 (a) XRD patterns of the precursor after milled, and the as-prepared samples (heat treatment at 110, 150, 200 and 260 °C for 24 h), the molar ratio of S to Se is 15:1, carbon content about 50%. (b,c) View of isostructural γ-sulfur phase of Se_xS_{8-x} ($x<4$) at different orientations. (d,e) The two distinct pairs of 8-membered rings in the unite cell. (f) XRD patterns of $S_{0.94}Se_{0.06}$ without the addition of carbon obtained at 260 °C for 24 h.

X-ray diffraction was utilized to investigate the phase transition with temperatures increasing, based on the sulphur-selenium binary phase diagram (Fig. S6).[23] There're only some weak peaks of Se after the milling process, as shown in Fig. 2a. When the precursor was heated at 110 °C, strong peaks of Se_xS_{8-x} ($x<4$, and not necessary to be an integer) with isostructural γ-sulfur phase appear.[24] As temperatures increased to 150 and 200 °C, there's an evolution from crystalline to amorphous state, indicating the impregnation of Se-S composites into the pores of porous carbon by capillary action.

The crystal structure of isostructural γ-sulfur phase Se_xS_{8-x} is shown in Fig. 2b,c, with two distinct pairs of 8-membered rings in the unite cell.[24] In one kind of 8-membered ring, the selenium and sulfur atoms appear struggled for all atomic positions (Fig. 2d). While in the other kind, apart from four such kind of atomic positions, there are four fixed atomic position are occupied by sulfur (Fig. 2e). Thus, in the isostructural γ-sulfur phase Se_xS_{8-x}, the selenium and sulfur atoms are not scrambled equally.[25, 26] And there might be composites with higher sulfur proportions once more atomic positions are occupied by S. Statistically, the homogeneous occupy of Se and S over the whole molecular guarantee the uniform distribution in the final amorphous $S_{0.94}Se_{0.06}$/C.

To further reveal the reaction between Se and S during the reaction process, we also obtain the samples with the same molar ratio of S to Se at 260 °C without the addition of carbon ($S_{1-x}Se_x$). The XRD pattern and XPS spectra of $S_{0.94}Se_{0.06}$ sample are shown in Fig. 2f and Fig. S7. The XRD patterns of other samples are also exhibited in Fig. S8, and all the diffraction peaks are similar to monoclinic phase of S_8 (JCPDS Card No. 71-0396, space group: P2/c). Moreover, the XPS spectra of S 2p and Se 3p of $S_{0.94}Se_{0.06}$ sample are overlap to each other, too. In addition, the Raman spectra of these four samples in Fig. S9 clearly exhibit the peaks of S-Se bond.

Electrochemical performance of the samples was examined in coin cells at room temperature, with carbonate-based electrolyte. For comparison, a sulphur–carbon composite (S/C) was also tested, synthesized by mixing sulphur powder and porous carbon with the same sulphur content about 50 wt%.

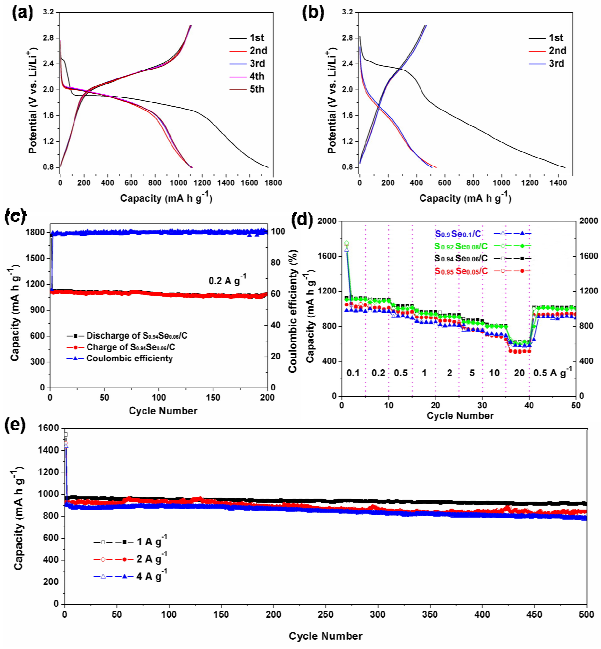

Fig. 3 (a,b) Typical galvanastatic discharge-charge curves of the cell with $S_{0.94}Se_{0.06}$/C and S/C electrodes in the potential region of 0.8–3 V versus Li/Li^+ at 0.2 A g^{-1}, respectively. (c) Cycling property and coulombic efficiency of the $S_{0.94}Se_{0.06}$/C electrode at constant current density of 0.2 A g^{-1}. (d) Cycle performance of $S_{1-x}Se_x$/C ($x \leq 0.1$) electrode at various current rates: 0.1, 0.2, 0.5, 1, 2, 5, 10, and 20 A g^{-1} and then back to 0.5 A g^{-1}. (e) Long-term cycling performance of $S_{0.94}Se_{0.06}$/C electrode at higher current density of 1, 2 and 4 A g^{-1}.

Fig. 3a shows discharge/charge voltage profiles of the $S_{0.94}Se_{0.06}$/C electrode at 0.2 A g^{-1} in the voltage window of 0.8–3.0 V. And the calculation of specific discharge/charge capacities is based on the total mass of elemental selenium and sulfur. During the first discharge process, an extremely small plateau at about 2.5 V appears, which was probably due to the formation of polysulfides/polysenelides.[17, 27] In the following cycles, the $S_{0.94}Se_{0.06}$/C electrode exhibits one discharge/charge plateau around 2.0 V, which is atributed to conversion of polysulfides to Li_2S and polyselenides to Li_2Se.[17] The first discharge and charge capacity of $S_{0.94}Se_{0.06}$/C electrode is 1755 and 1106 mA h g^{-1}, respectively, with initial Coulombic efficiency of ~63%. While, for the profiles of the S/C sample (Fig. 3b), $S_{0.94}Se_{0.06}$ sample (Fig. S10) and $S_{0.94}Se_{0.06}$/C samples obtained at low temperature (Fig. S11), the plateau of ~2.4 V in the first discharge is the dominate one, and those samples cannot be fully reduced in the subsequent cycles, especially for the $S_{0.94}Se_{0.06}$ sample. Thus, it is suggested that both the introducing of Se and the fully impregnation Se-S into carbon host is important for reduce the formation of large polysulfides.

From the second cycle onwards, the Coulombic efficiency of $S_{0.94}Se_{0.06}$/C electrode increases and reaches nearly 100% after several cycles as shown in Fig. 3c, suggesting the diminished shuttling effect[28]. After deep cycling for 200 cycles, a high capacity of 1090 mA h g^{-1} can still be retained corresponding to a high capacity retention of 98.6% from the second cycle. The cycling is also quite stable at higher rate of 1, 2 and 4 A g^{-1}, with stable capacity of 910, 851 and 792 achieved after 500 cycles (Fig. 3e). And good rate capability [29] and long cycling stability [30,31] are both critical for practical application in energy storage systems. The cycling performance of other three samples with different molar proportion of S ($S_{0.9}Se_{0.1}$/C, $S_{0.92}Se_{0.08}$/C, $S_{0.95}Se_{0.05}$/C) were also investigated as shown in Fig. S12, from which one can see that the cycling stabilities of those samples are good. Moreover, the cycling performance of S/C composites is shown in Fig. S13, which shows much lower capacity and inferior cycling stability. On the other hand, as can be seen in the Raman spectra of those $S_{1-x}Se_x$/C ($x \approx 0.1$, 0.08, 0.06, 0.05) electrodes (the dis-assembled electrodes were dissolved in CS_2 solution) at charge state after 100 cycles at 0.5 A g^{-1} in Fig. S14, the peaks of S-Se, S-S bonds, and skeleton deformation of Se_nS_{8-n} system still remained even the intensity is weakened. Thus, it can be inferred that the introducing low proportional Se could anchor S during cycling, and effectively reduce the dissolution of polysulfides and shuttle effect.

The $S_{0.94}Se_{0.06}$/C sample also shows excellent cycling response to continuously varying current densities, as shown in Fig. 3d. The discharge capacity varies from 1123, 1105, 1034, 961, 926, 863, 802 to 617 mA h g^{-1} with the increasing current rate from 0.1, 0.2, 0.5, 1, 2, 5, 10 to 20 A g^{-1}, respectively. The capacity then increases back to 1018 mA h g^{-1} when return the current density back to 0.5 A g^{-1}. The other three $S_{1-x}Se_x$/C samples exhibit similar performance and maintains capacity about 493~605 mA h g^{-1} at current rate of 20 A g^{-1} (Fig. 3d). On the other hand, for the consideration of practical application [32], the electrochemical performance of $S_{0.94}Se_{0.06}$/C electrodes with higher loading or with less carbon host was shown in Fig. S15a-d. The corresponding electrochemical performance was not as good as that shown in Fig. 3, which need further improvement from the perspective of high energy density cells. It is believed that the introduced selenium with higher conductivity could improve the sluggish kinetics and poor conductivity of sulfur cathodes.[16] More direct evidence based on the electrochemical impedance spectroscopy (EIS) analysis is shown in Fig. S16 and Table S2. The results demonstrate that the electrical conductivity of the $S_{1-x}Se_x$/C composite cathodes

increases significantly along with the increase of the content of Se, and the resistance of S/C sample without Se is the highest among the samples. And those data are consistent with the trend of better rate capability along with higher Se content in the composites.

On the other hand, the EIS was also employed to demonstrate the stable long-term charge-discharge performance of the $S_{0.94}Se_{0.06}$/C electrode, and the cell impedance of the $S_{0.94}Se_{0.06}$/C composite electrode in the full charge state after the cycle from 1 to 50 have been detected (Fig. 4a). Based on previous reports, there might be a "solid electrolyte interface (SEI)" similar to Li-ion batteries on the SeS_x/C cathodes in carbonate electrolyte [17,33]. During the cycling at 0.2 A g^{-1}, the $S_{0.94}Se_{0.06}$/C composite electrode at their full charge state exhibited a relatively stable SEI layer and reversible electrochemical process, from which the resistances of the electrolyte (R_s), SEI layer (R_{SEI}) and charge transfer in electrode material (R_{ct}) are stable around 2.8, 3, and 70 Ω, respectively (Fig. 4b). Compared with the previous reported of the S cathode, the $S_{0.94}Se_{0.06}$/C composite electrode shows more stable impedances and better cycle stability, smaller impedances and greater rate capacity.

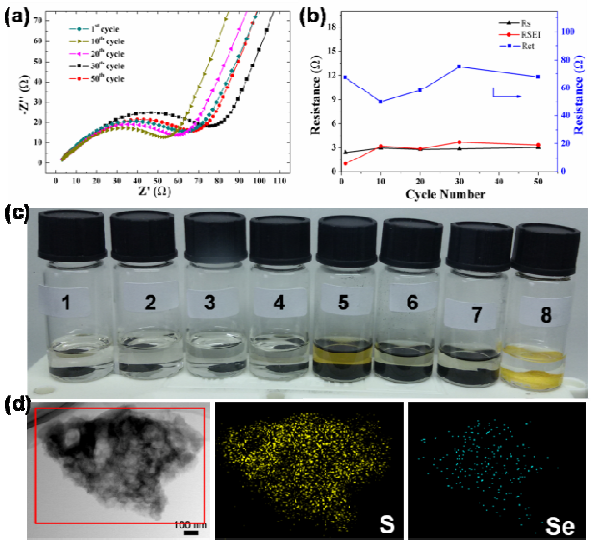

Fig. 4 (a) Cell impedance tests of the $S_{0.94}Se_{0.06}$/C electrode in the full charge state after the cycle from 1 to 50. (b) The impedance of the electrolyte resistance (R_s), surface SEI layers (R_{SEI}) and charge transfer (R_{ct}) of the $S_{0.94}Se_{0.06}$/C electrode during cycling. (c) Photograph of carbonate-based electrolyte with $S_{0.94}Se_{0.06}$/C electrode charged to (1) 2.172 V, (2) 3.0 V, discharged to (3) 1.986 V, (4) 0.8 V, (5) the precursor after ball-milled, (6) the S/C composite, (7) the $S_{0.94}Se_{0.06}$/C sample and (8) the $S_{0.94}Se_{0.06}$ without carbon (about 0.02 mol L^{-1}) after 10 days. (d) TEM image and Se, S elemental mapping of $S_{0.94}Se_{0.06}$/C electrode after 500 cycles.

Furthermore, we tested the solubility of the $S_{0.94}Se_{0.06}$/C composites in the carbonate electrolyte, as comparison, those of S/C, the raw materials of S, Se and porous carbon after ball-milled and the $S_{0.94}Se_{0.06}$ without carbon immersed in the carbonate electrolyte for 10 days were also tested, as shown in Fig. 4c. No color change was observed for the samples of $S_{0.94}Se_{0.06}$/C and $S_{0.94}Se_{0.06}$, while the raw materials after ball-milled changed from colorless to yellow-green. And the S/C sample also exhibits a faint yellow color. These phenomena give a hint that Se-S bond in $S_{1-x}Se_x$ composites may be favorable for their chemical stability in the electrolyte.

To understand the lack of dissolution of any intermediate phases during cycling, we took images of $S_{0.94}Se_{0.06}$/C electrodes at four different charge/discharge degrees (Fig. 4c). There's no obvious color change for these four electrodes. ICP-OES (Inductively coupled plasma-Optical emission spectrometer) measurement was also used to estimate the total sulfur content dissolved in electrolytes [34]. And there's almost no sulfur in the electrolyte for those four electrodes. Those results clearly demonstrate the ability of Se to restrict the intermediate dissolution and the successful spatial confinement effect of porous carbon host, leading to the super cycling stability reflected by cyclic voltammetry curves after 300 cycles in Fig. S17. In addition, Se, S elemental mapping (Fig. 4d) and overall morphology (Fig. S18) of $S_{0.94}Se_{0.06}$/C electrode after 500 cycles were also investigated, which demonstrate the similar uniform distribution to that of the original material. The EDS analysis showed that the S/Se ratio was about 15 for the $S_{0.94}Se_{0.06}$/C electrode after cycling, which was consistent with that of the raw $S_{0.94}Se_{0.06}$/C electrode.

In summary, we have obtained a series of S-rich $S_{1-x}Se_x$/C ($x \leq 0.1$) composites starting from Se and S powders at 260 °C. As cathodes for Li-S batteries, the $S_{1-x}Se_x$/C exhibit much higher reversible capacity, better stability and rate capability in carbonate-based electrolyte. The introducing of low proportional Se together with the confinement effect of porous carbon may restrict the dissolution of S cathodes during cycling, and contribute to the high electrochemical performance. The present study provides an effective and feasible approach, which bring the Li–S battery a step closer to practical realization.

Experimental

Synthesis of porous carbon

The synthesis of porous carbon here is similar to our previous work [35], which is opposite to the common sacrificial template method [36] (porous carbon is the target product in our procedure rather than template). In a typical synthesis, 5 mmol of $MnCl_2 \cdot H_2O$ and 5 mmol of malic acid were added into 40 mL ethanol in a 100 mL beaker. Then, 4 mL of 2.5 M NaOH was added to the above solution dropwise. Finally, the beaker was sealed and maintained for 6 h with the help of ultrasonication. The pink product was filtered and washed with deionized water and ethanol several times, dried under vacuum at 60 °C for 6 h. The as-prepared precursor was heated at 700 °C for 5 h in Ar atmosphere (heating rate 5 °C min^{-1}) followed by the washing process with diluted HNO_3 and deionized water.

Synthesis of S-rich $S_{1-x}Se_x$/C composites

Se and S were loaded into the porous carbon by a melting-diffusion method. Typically, the porous carbon was ball-milled with commercial selenium and sulfur powder (the molar ratio of S to Se ranging from 9 to 18) and the carbon content is about 50wt%. Then the mixture was fully filled in a 5 ml

Teflon-lined stainless steel autoclave, heated at 110, 150, 200 and 260 °C for 24 h and then cooled to room temperature naturally. For the $S_{1-x}Se_x$ composites without carbon, the preparation procedure is similar, except the adding of porous carbon.

Synthesis of S/C composites

S was loaded into the porous carbon by a melting-diffusion method. Typically, the porous carbon was ball-milled with commercial sulfur powder with carbon content about 50wt%. Then the mixture was fully filled in a 5 ml Teflon-lined stainless steel autoclave, heated at 155 °C for 24 h and then cooled to room temperature naturally.

Material Characterization

The morphology of the reaction product were characterized by scanning electron microscopy (SEM, JEOL-JSM-6700F), transmission electron microscopy (TEM), scanning transmission electron microscopy (STEM) images and energy dispersive spectroscope (EDS) analysis were digitally acquired using a field emission JEM-ARM 200F TEM with the as-prepared samples disperse on 200 mesh lacey-carbon copper TEM grids. X-ray diffractometer (XRD) was carried out on a Philips X' Pert Super diffract meter with Cu Kα radiation (λ=1.54178 Å). Raman spectrum was performed with 514.5 nm wavelength. XPS were recorded on an ESCALAB 250 spectrometer (Perkin-Elmer) to characterize the surface composition. The carbon and sulphur content of the product was check by EA (Vario EL-III) and to check the compositions. The Brunauer- Emmett-Teller (BET) surface area and Barrett-Joyner-Halenda (BJH) pore distribution plots were measured on a Micromeritics ASAP 2020 accelerated surface area and porosimetry system. The Inductively coupled plasma-Optical emission spectrometer (ICP-OES) measurement was conducted on Optima 7300 DV system.

Electrochemical Measurement

The electrochemical properties of the $S_{1-x}Se_x$/C electrodes were measured with coin-type half cells (2016 R-type) which assemble under an argon-filled glove box (H_2O, O_2 < 1 ppm). Working electrode was prepared by mixing the $S_{1-x}Se_x$/C composites, super P carbon black and sodium alga acid (SA) binder in a weight ratio of 70:20:10 in water solvent. The slurry was pasted onto an Al foil and then dried in a vacuum oven at 60 °C for 15 h. The active material density of each cell was determined to be 0.8-1.5 mg cm^{-2}. Metallic Li sheet was used as counter electrode, and 1 M $LiPF_6$ in a mixture of ethylene carbonate/dimethylcarbonate (EC/DMC; 1:1 by Volume) as the electrolyte (Zhuhai Smoothway Electronic Materials Co., Ltd (china)). The amount of electrolyte is about 100 µL in each cell during assembling. Galvanostatic measurements were made using a LAND-CT2001A instrument at room temperature that was cycled between 0.8 V and 3.0 V versus Li^+/Li at different current density from 0.1 to 20 A g^{-1}. The AC impedance spectra were carried out on an electrochemical workstation (CHI660E) by applying an AC voltage of 5 mV in amplitude in the frequency range of 0.01 Hz to 100 kHz at room temperature. The obtained spectra were analyzed using ZView software. The calculation of specific discharge/charge capacities is based on the total mass of elemental selenium and sulfur.

Acknowledgements

This work was financially supported by the 973 Project of China (No. 2011CB935901), the National Natural Science Fund of China (No. 21471142, 21201158).

Notes and references

1. D. Herbert and J. Ulam, U.S. Patent, 3043896, 1962.
2. Y. Yang, G. Zheng and Y. Cui, *Chem. Soc. Rev.*, 2013, **42**, 3018-3032.
3. A. Manthiram, Y. Fu, S.-H. Chung, C. Zu and Y.-S. Su, *Chem. Rev.*, 2014, **114**, 11751-11787.
4. J. Zheng, J. Tian, D. Wu, M. Gu, W. Xu, C. Wang, F. Gao, M. H. Engelhard, J.-G. Zhang and J. Liu, *Nano Lett.*, 2014, **14**, 2345-2352.
5. G. Zhou, S. Pei, L. Li, D. W. Wang, S. Wang, K. Huang, L. C. Yin, F. Li and H. M. Cheng, *Adv. Mater.*, 2014, **26**, 625-631.
6. J. Song, T. Xu, M. L. Gordin, P. Zhu, D. Lv, Y. B. Jiang, Y. Chen, Y. Duan and D. Wang, *Adv. Funct. Mater.*, 2014, **24**, 1243-1250.
7. S. Moon, Y. H. Jung, W. K. Jung, D. S. Jung, J. W. Choi and D. K. Kim, *Adv. Mater.*, 2013, **25**, 6547-6553.
8. X. Liang, C. Hart, Q. Pang, A. Garsuch, T. Weiss and L. F. Nazar, *Nat. Commun.*, 2015, **6**.
9. X. Tao, J. Wang, Z. Ying, Q. Cai, G. Zheng, Y. Gan, H. Huang, Y. Xia, C. Liang and W. Zhang, *Nano Lett.*, 2014, **14**, 5288-5294.
10. Y. Yang, G. Yu, J. J. Cha, H. Wu, M. Vosgueritchian, Y. Yao, Z. Bao and Y. Cui, *Acs Nano*, 2011, **5**, 9187-9193.
11. H. J. Peng, J. Q. Huang, M. Q. Zhao, Q. Zhang, X. B. Cheng, X. Y. Liu, W. Z. Qian and F. Wei, *Adv. Funct. Mater.*, 2014, **24**, 2772-2781.
12. X. Ji, K. T. Lee and L. F. Nazar, *Nat. Mater.,* 2009, **8**, 500-506.
13. X. Liang, A. Garsuch and L. F. Nazar, *Angew. Chem., Int. Ed*, 2015, **54**, 3907-3911.
14. S. Xin, L. Gu, N.-H. Zhao, Y.-X. Yin, L.-J. Zhou, Y.-G. Guo and L.-J. Wan, *J. Am. Chem. Soc.*, 2012, **134**, 18510-18513.
15. A. Abouimrane, D. Dambournet, K. W. Chapman, P. J. Chupas, W. Weng and K. Amine, *J. Am. Chem. Soc.*, 2012, **134**, 4505-4508.
16. Y. Cui, A. Abouimrane, J. Lu, T. Bolin, Y. Ren, W. Weng, C. Sun, V. A. Maroni, S. M. Heald and K. Amine, *J. Am. Chem. Soc.*, 2013, **135**, 8047-8056.
17. C. Luo, Y. Zhu, Y. Wen, J. Wang and C. Wang, *Adv. Funct. Mater.*, 2014, **24**, 4082-4089.
18. C. Hoffmann, S. Thieme, J. Brückner, M. Oschatz, T. Biemelt, G. Mondin, H. Althues and S. Kaskel, *ACS nano*, 2014.
19. H.-J. Peng, J. Liang, L. Zhu, J.-Q. Huang, X.-B. Cheng, X. Guo, W. Ding, W. Zhu and Q. Zhang, *ACS nano*, 2014, **8**, 11280-11289.
20. B. Wang, Y. Wen, D. Ye, H. Yu, B. Sun, G. Wang, D. Hulicova‐Jurcakova and L. Wang, *Chem. Eur. J.*, 2014, **20**, 5224-5230.

21. H. Eysel and S. Sunder, *Inorg. Chem.*, 1979, **18**, 2626-2627.
22. R. Steudel and E. M. Strauss, *Angew. Chem., Int. Ed*, 1984, **23**, 362-363.
23. W. Ringer, *Z. Anorg. Chern.*, 1902, **32**, 183-218.
24. R. A. Boudreau and H. M. Haendler, *J. Solid State Chem*, 1981, **36**, 289-296.
25. J. Taavitsainen, H. Lange and R. S. Laitinen, *J.Mol.Struct.: THEOCHEM*, 1998, **453**, 197-208.
26. R. S. Laitinen and T. A. Pakkanen, *Inorg. Chem.*, 1987, **26**, 2598-2603.
27. Z. Li, L. Yuan, Z. Yi, Y. Liu and Y. Huang, *Nano Energy*, 2014, **9**, 229-236.
28. W. Zhou, H. Chen, Y. Yu, D. Wang, Z. Cui, F. J. DiSalvo and H. D. Abruña, *ACS nano*, 2013, **7**, 8801-8808.
29. J. Wang, N. Yang, H. Tang, Z. Dong, Q. Jin, M. Yang, D. Kisailus, H. Zhao, Z. Tang and D. Wang, *Angew. Chem.*, 2013, **125**, 6545-6548.
30. H. Tang, J. Wang, H. Yin, H. Zhao, D. Wang and Z. Tang, *Adv. Mater.*, 2015, **27**, 1117-1123.
31. H. Ren, R. Yu, J. Wang, Q. Jin, M. Yang, D. Mao, D. Kisailus, H. Zhao and D. Wang, *Nano Lett.*, 2014, **14**, 6679-6684.
32. M. Hagen, D. Hanselmann, K. Ahlbrecht, R. Maça, D. Gerber and J. Tübke, *Adv. Energy Mater.*, 2015, **5**, 1401986.
33. Y. Xu, Y. Wen, Y. Zhu, K. Gaskell, K. A. Cychosz, B. Eichhorn, K. Xu and C. Wang, *Adv. Funct. Mater.*, 2015, **25**, 4312–4320.
34. Y. Diao, K. Xie, S. Xiong and X. Hong, *J. Electrochem. Soc.*, 2012, **159**, A421-A425.
35. X. Li, X. Zhu, Y. Zhu, Z. Yuan, L. Si and Y. Qian, *Carbon*, 2014, **69**, 515-524.
36. Z. Dong, H. Ren, C. M. Hessel, J. Wang, R. Yu, Q. Jin, M. Yang, Z. Hu, Y. Chen and Z. Tang, *Adv. Mater.*, 2014, **26**, 905-909.

Table of contents

Amorphous S-rich $S_{1-x}Se_x/C$ ($x \leq 0.1$) Composites Promise Better Lithium Sulfur Batteries in Carbonate-based Electrolyte

Xiaona Li, Jianwen Liang, Kailong Zhang, Zhiguo Hou, Wanqun Zhang, Yongchun Zhu,* and Yitai Qian*

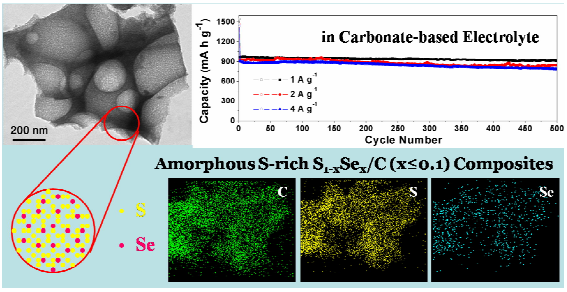

The low electrochemical utilization of S and fast capacity fading can be effectively diminished by immobilize sulfur in porous carbon via the interaction of a small amount of selenium in S-rich $S_{1-x}Se_x$ /C ($x \leqslant 0.1$) composites.